Journal of Materials Chemistry A

Accepted Manuscript

ROYAL SOCIETY OF CHEMISTRY

www.rsc.org/materialsA

Journal of Materials Chemistry A

PAPER

Integrated Cobalt Disulfide (CoS_2) Co-catalyst Passivation Layer on Silicon Microwires for Photoelectrochemical Hydrogen Evolution

Received 00th January 20xx,
Accepted 00th January 20xx

DOI: 10.1039/x0xx00000x

www.rsc.org/

Chih-Jung Chen,[a] Po-Tzu Chen,[b] Mrinmoyee Basu,[a] Kai-Chih Yang,[b] Ying-Rui Lu,[cd] Chung-Li Dong,[c] Chong-Geng Ma,[e] Chin-Chang Shen,[f] Shu-Fen Hu*[b] and Ru-Shi Liu*[ag]

Integrated cobalt disulfide (CoS_2) co-catalyst passivation layer on Si microwires (MWs) were used as a photocathode for solar hydrogen evolution. Si MWs were prepared by photolithography and dry etching technique. The CoS_2-Si photocathodes were subsequently prepared by chemical deposition and thermal sulfidation of the $Co(OH)_2$ outer shell. The optimized onset potential and photocurrent of the CoS_2-Si electrode were 0.248 V and −3.22 mA cm^{-2} (at 0 V), respectively. The best photocatalytic activity of the CoS_2-Si electrode resulted from lower charge transfer resistances among the photoabsorber, co-catalyst, and redox couples in the electrolyte. X-ray absorption near edge structure was conducted to investigate the unoccupied electronic states of the CoS_2 layer. We propose that more vacancies in the S-3p unoccupied states of the CoS_2-Si electrode were present with a lower negative charge of S_2^{2-} to form weaker S–H bond strength, promoting water splitting efficiency. Moreover, the CoS_2 co-catalyst that completely covered underlying Si MWs, was served as a passivation layer to prevent oxidation and reduce degradation during photoelectrochemical measurements. Therefore, the optimal CoS_2-Si electrode maintained the photocurrent at about −3 mA cm^{-2} (at 0 V) for 9 h, and its hydrogen generation rate was approximately 0.833 μmol min^{-1}, respectively.

Introduction

At present, the annual global energy consumption rate is about 15 TW, and it is estimated to increase to 25–27 TW by 2050.[1] In 2011, approximately 81% of the worldwide energy requirement was met utilizing fossil fuels. However, relying on fossil fuels leads to 30.4 Gt carbon dioxide emission, resulting in serious greenhouse effect and global warming.[2] Solar light, an infinite energy source, is received by Earth with an approximate rate of 120,000 TW per year.[1] Efficient harvest of solar irradiation for energy generation is an optimized candidate for solving the energy crisis. In 1972, Honda and Fujishima first demonstrated the conversion of solar energy into chemical fuels through splitting water.[3] Various semiconductor materials have been employed to develop a highly efficient photocatalyst or photoelectrode. Silicon (Si) with a highly negative conduction band edge (ca. −0.46 V vs. NHE) and small band gap (1.1 eV) has been functioned as the most promising photocathode material for solar hydrogen production. However, low hydrogen evolution reaction (HER) kinetics on Si surfaces have led to efforts of noble Pt co-catalyst modification, which is used as catalytic electron collectors to decrease recombination.[4-6] In our previous research, Ag-Si microflowers were prepared as a photocathode for the hydrogen generation reaction by a facile chemical method.[7] The optimized photocurrent of Ag-Si electrodes was −35 mA cm^{-2} at −1.0 V (vs. Ag/AgCl), and its hydrogen evolution rate (HER) reached 8.3 μmol min^{-1} by the synergetic effect of Ag co-catalyst and plasmonic assistance. However, these high-cost metal materials limit the large-scale deployment and practical applications because of its rare storage in Earth.[8]

The research group of N. S. Lewis previously demonstrated that the earth-abundant Ni–Mo alloy coated-Si microwires, which were prepared by the a vapor-liquid-solid (VLS) method, shows high efficiencies for solar hydrogen generation.[9, 10] In our previous study, marcasite $CoSe_2$ nanorods was prepared through hydrothermal reaction, and subsequently spin-coated on Si microwire arrays as a high efficiency photocathode.[11] However, $CoSe_2$ nearly aggregated on tops of Si microwires, and the major restriction of using Si material for solar water splitting is easy oxidation to electrically insulating SiO_2 after electrolyte exposure.[12] The oxidized Si electrodes reduce photogenerated carriers to migrate to its surface and result in serious degradation

[a] Department of Chemistry, National Taiwan University, Taipei 10617, Taiwan. E-mail: rsliu@ntu.edu.tw
[b] Department of Physics, National Taiwan Normal University, Taipei 11677, Taiwan. E-mail: sfhu.hu@ntnu.edu.tw
[c] National Synchrotron Radiation Research Center, Hsinchu 30076, Taiwan.
[d] Program for Science and Technology of Accelerator Light Source, National Chiao Tung University, Hsinchu 30010, Taiwan.
[e] College of Sciences, Chongqing University of Posts and Telecommunications, Chongqing 400065, China.
[f] Institute of Nuclear Energy Research, Atomic Energy Council, Taoyuan 32546, Taiwan.
[g] Department of Mechanical Engineering and Graduate Institute of Manufacturing Technology, National Taipei University of Tech-nology, Taipei 10608, Taiwan.
Electronic Supplementary Information (ESI) available: [details of any supplementary information available should be included here]. See DOI: 10.1039/x0xx00000x

or deactivation. Therefore, methyl functional groups were applied to protect Si from oxidation through a two-step halogenation/alkylation reaction. Mixed methyl/allyl monolayer-modified Si showed comparable passivation performance as CH_3-Si while allowing facile secondary surface functionalization. However, the durability of these organic materials for long periods remains unclear.[13, 14] The monolayer graphene, prepared by chemical vapor deposition (CVD), was also employed on Si photocathodes to suppress oxidation. Besides, nitrogen-doped and defect abundant graphene, fabricated through N_2 plasma treatment, decreased the overpotential of Si electrodes to further enhance its performance. The photocurrent at 0 V versus RHE (pH = 0) of N-doped graphene-decorated Si still decayed by about 70% within 10,000 s.[15] Amorphous molybdenum sulfide (MoS_x) or titanium oxide (TiO_2) were incorporated with titanium-protected n^+p-Si photocathode for improved water splitting stability, whereas the depth of titanium native oxide gradually increased with long-term measurement.[12, 16] In addition, the titanium thin film oxidized to thermodynamically stable $Ti^{3+}_{(aq)}$ and $Ti^{2+}_{(aq)}$ ions at voltages below −0.315 and −0.528 V versus NHE in acidic media (pH = 0). Thus, an integrated MoS_2 passivation and catalytic layer was directly deposited on the n^+p-Si electrode, carrying out solar hydrogen generation at 0 V versus RHE for more than 5 days without degradation.[17] Recently, amorphous MoS_xCl_y thin film was deposited on p-type Si photocathode to achieve high cathodic current −20.6 mA cm^{-2} at 0 V (vs. RHE).[18] Inspired from these previous studies, the photocatalytic durability of the Si electrode can be improved by integrating electrochemically stable materials.

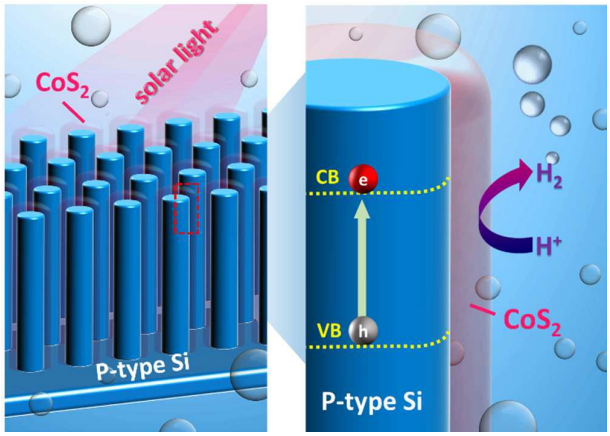

Fig. 1 Schematic illustration of CoS_2 co-catalyst passivation layer-decorated Si microwires photocathode.

Recently, Earth-abundant inorganic electrocatalysts play key roles in the conversion of renewable energy.[19] Among various non-noble electrocatalysts, cubic pyrite-phase transition metal dichalcogenides (with the general formula MX_2, where M = Fe, Co, or Ni and X = S or Se) showed promising efficiencies for electrolytic hydrogen evolution.[20-24] Among numerous metal disulfides, CoS_2 particles revealed the lowest cathodic overpotential (−128 mV vs. RHE) to drive the HER at 1 mA cm^{-2}.[24] Besides, amorphous cobalt sulfide (Co-S) film was prepared via electrochemical deposition, and it had low catalytic onset overpotential and approximately 100% Faradaic efficiency in pH 7 phosphate buffer.[25] In the presented work, electrochemically stable cobalt disulfide (CoS_2) was selected as a co-catalyst passivation layer to decorate on Si microwires (MWs) as a photocathode for solar water splitting, as shown in Figure 1. The optimized photocurrent of CoS_2-Si MWs was -3.22 mA cm^{-2} at 0 V (vs. RHE), and linear sweep voltammograms (LSV) were measured through 30 scans without variations. Moreover, chronoamperometry was carried out at 0 V (vs. RHE) for 9 h with no degradation, and its hydrogen generation rate were 0.833 μmol min^{-1}, respectively. These results showed that the CoS_2 passivation layer was extremely robust in protecting Si MWs from oxidation.

Experimental

Fabrication of Si MW arrays.

Si MW arrays were fabricated through the photolithography technique and dry etching system, as shown in Fig. 2. The boron-doped p-type (100)-oriented Si wafers (resistivity: 1–25 Ω cm) were selected for the preparation of Si MWs. First, Si wafers were cleaned by STD method and diluted hydrogen fluoric acid (HF) solution. The wet oxide (SiO_2), which functioned as a hard mask, was grown on Si wafers through low-pressure chemical vapor deposition (LPCVD). The photoresistant layer with a thickness of 800 nm was deposited on the wet oxide by spin coating. After the exposure and development of the photoresist by photolithography technique, the patterns were defined as square arrays with 1.7 μm pitch size. The revealing SiO_2 hard mask was then removed under a mixed atmosphere of CHF_3, CF_4, and Ar by TE5000 dry etching. The O_2 plasma was applied to eliminate the photoresist under a pressure of 1.1 torr at 250 °C by Mattson AspenII Asher. Si MWs were subsequently prepared using inductively coupled plasma-reactive ion etching (ICP-RIE) with an etching rate of 2 μm min^{-1} under SF_6 and O_2 atmosphere, and immersed in diluted HF acid solution for 60 s to remove residual SiO_2 hard masks. The back side of the Si MWs was polished until the total thickness was 350 μm. An e-gun evaporator system was then conducted to deposit the Al metal with 500 nm thickness, which functioned as a back electrode.

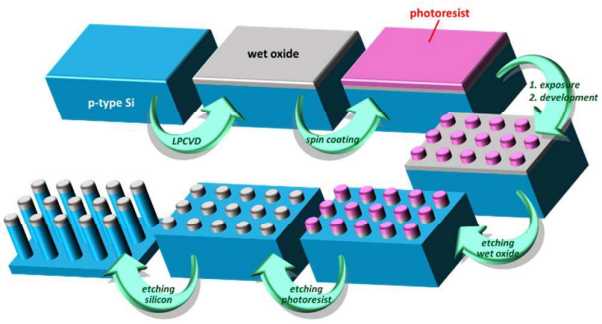

Fig. 2 Schematic illustration of fabrication procedure of Si microwire arrays.

Fabrication of $Co(OH)_2$-Si MW arrays.

The $Co(OH)_2$ synthesis method was followed a previous work.[22] $Co(OH)_2$-Si MW arrays were prepared by a facile chemical reaction. The Al back electrode of the Si MW arrays was covered with Teflon tape, which functioned as a mask during the chemical reaction. Si MWs were then fixed on a microscopic slide. Cobalt nitrate hexahydrate [$Co(NO_3)_2$•$6H_2O$] (2.91 g) was dissolved in 10 mL of deionized (DI) water to prepare 10 mmol precursor solution. About 40 mL of concentrated ammonia (NH_4OH) solution (30%–33%) was then slowly added dropwise into the precursor solution under vigorous stirring. After adding $NH_4OH_{(aq)}$, the final solution was further stirred for 30 min and then poured in a cap of a Petri dish. The microscopic slide with Si MWs was upside down to immerse in the mixed solution, and kept approximately 2 mm from the bottom of the Petri dish. Another cap of a Petri dish covered on its top was then heated to 85 °C through an oven for the desired duration. After the reaction, the $Co(OH)_2$-deposited-Si MWs were rinsed by DI water and blown dry with a nitrogen gun.

Fabrication of CoS_2-Si MW arrays.

CoS_2-Si MW arrays were prepared by thermal sulfidation of $Co(OH)_2$-Si MWs. The as-prepared $Co(OH)_2$-Si MW arrays and 2 g of sulfur powder were separately placed in different alumina crucibles. The crucible with $Co(OH)_2$-Si MWs was placed at the middle of alumina tube furnace, and another crucible with sulfur powder was placed at the upstream position. The crucibles were heated to 500 °C at a rate of 5 °C min^{-1} and held for 1 h under Ar atmosphere with a flow rate of 30–40 mL min^{-1}. The tube furnace was then naturally cooled down to room temperature.

Fabrication of Pt-Si MW arrays.

Pt-Si MW arrays were synthesized through chemical electroless deposition. The Cu wire was mounted on the Al back electrode of Si MWs using Ag paste and subsequently covered with an electronic insulating epoxy, which functioned as a mask to avoid the Al back electrode from being etched. About 80 mL of HF acid (1 M) and H_2PtCl_6 (10 mM) mixed aqueous solution was prepared in a Teflon beaker. The Si MW electrode was then immersed in this reaction solution for 180 s. After electroless deposition of Pt NPs, the electrode was rinsed by DI water and dried with a nitrogen gun.

Photoelectrochemical measurement.

The Al back electrode of the as-synthesized photocathode was stuck Cu wire through the Ag paste and then heated to dryness at 60 °C in the oven. The electronic insulating epoxy was subsequently coated on the photocathode to prevent the undesirable dark current. The photoelectrochemical cell was composed of the three-electrode system, and it was surrounded with the circulation water to maintain the temperature at 25 °C. The as-prepared photocathode functioned as the working electrode. Moreover, the saturated Ag/AgCl electrode and Pt plate were the reference and counter electrodes, respectively. Before conducting the photoelectrochemical measurement, Pt plate was cleaned by concentrated sulfuric acid to remove the surface contamination. Sulfuric acid solution (0.5 M, 250 mL) was prepared as the electrolyte. All photoelectrochemical characterizations were carried out under the illumination of a xenon lamp equipped with an AM 1.5 filter, and the light intensity was constant at 100 mW cm^{-2}. The linear sweep voltammograms (LSV), incident photon-to-electron conversion efficiency (IPCE), chronoamperometry, and gas evolution data were recorded using a potentiostat (Eco Chemie AUTOLAB, The Netherlands) and General Purpose Electrochemical System (GPES) software. LSV measurements were conducted from 0.5 V to −0.45 V with a scan rate of 20 mV s^{-1}. IPCE, chronoamperometry, and gas evolution were carried out at 0 V. Electrochemical impedance spectroscopy (EIS) data was measured by an electrochemical workstation (760D, CH Instruments) under solar simulation with an applied bias of 0.4 V. The sweeping frequency was conducted from 560 kHz to 20 Hz with a 10 mV amplitude.

Characterization of materials.

Scanning electron microscopy (SEM) images were collected by utilizing a JEOL JSM-6700F field-emission SEM to observe the morphologies of the photocathodes. The crystallization and absorption range of the photocathodes were characterized through a Bruker D2 PHASER X-ray diffraction (XRD) analyzer with Cu Kα radiation (λ = 1.54178 Å) and a Thermo EVOLUTION 220 spectrometer, respectively. Raman spectra were collected using a Thermo DXR microscope with a 532 nm laser. The X-ray photoelectron spectroscopy (XPS) spectra were performed through a PHI Quantera surface analyzer with Al Kα radiation (λ = 8.3406 Å). The X-ray absorption spectroscopy (XAS) experiments were conducted at the 20A1 and 16A1 beamlines of the National Synchrotron Radiation Research Center (NSRRC) in Hsinchu City, Taiwan.

Theoretical computational calculations.

The structural and electronic properties of the CoS_2 bulk materials were calculated by the periodic ab initio CRYSTAL09 code[26] using the local Gaussian-type basis sets. To exhibit the open shell character of $3d^7$ configuration of Co^{2+} ions in the compound, we considered the spin-polarized solutions to the present DFT calculations, and the spin value of each Co^{2+} ion was locked to 1/2 in the first eight cycles of the self-consistent field (SCF) calculations. The hybrid exchange-correlation functional WC1PBE[27] was used in this work because of its positive performance in our previous work[11]. The all-electron basis sets 86-411d41G and 86-311d1G were chosen for cobalt[28] and sulfur[29] atoms, respectively. The basis set optimization by the improved "Billy" script[30] was carried out to further decrease the total energy of our studied system. In all the SCF calculations,

we adopted an 8×8×8 k-point mesh[31] in the Brillouin zone and set the truncation criteria of the bielectronic integrals (Coulomb and HF exchange series) as 8, 8, 8, 8, and 16. A predefined "extra extra large" pruned DFT integration grid was chosen for high accuracy. The energy convergence threshold of the SCF iterations was set to 10^{-9} Hartree, and the Anderson mixing scheme with 50% mixing was used to improve the convergence speed. The convergence thresholds of the root-mean-square of the gradient and nuclear displacement for the geometry optimization were set to 0.00006 Hartree/bohr and 0.00012 bohr, respectively.

Results and discussion

In this study, Si MWs were fabricated by photolithography technique and dry etching system, as shown in Figure 2 (see details in Experimental section). The scanning electron microscopy (SEM) images revealed that the pitch size of the Si MW arrays was ~2 μm, and the diameter and length of a single wire were 1 and 10 μm, as shown in Figure 3a and 3c, respectively. Compared with Si planar structures, the light absorption and surface area of the Si MWs were both increased to enhance its photoresponse. Moreover, the one-dimensional structure of Si MWs provided shorter diffusion lengths for minority carriers and single conductive direction for majority carriers to reduce recombination. The CoS_2-Si photocathodes were prepared through chemical deposition and thermal sulfidation of $Co(OH)_2$. For convenience, we abbreviated Si MWs with different CoS_2 loading amounts as "CoS_2-Si-T," in which T (nm) represents the thickness of CoS_2. Figure S1a reveals that the diameters of CoS_2-Si-200 increased to ~1.4 μm compared with the pristine Si MWs, and CoS_2-Si-250 MWs had a diameter of ~1.5 μm, as shown in Figure 3b. However, further extending the thickness of CoS_2 layer resulted in single CoS_2-Si MW cross-linked the others in Figure S1b and S1c. Figure 3d also presents that this chemical deposition method fully coated all of the Si MW surfaces with the CoS_2 layer. Low-magnification top-view SEM images showed that the CoS_2 outer shell uniformly covered on Si MWs without by-product particles aggregated on top, as illustrated in Figure S2. Besides, the SEM elemental mapping of CoS_2-Si-250 MWs in Figure S3 revealed that the CoS_2 outer shell was uniformly distributed on the Si inner cores.

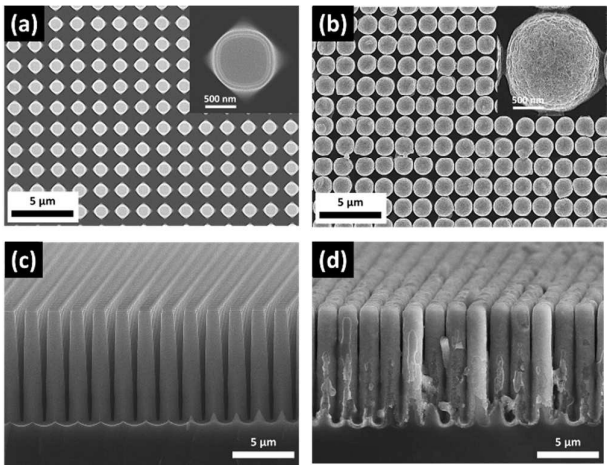

Fig. 3 (a,b) Top view and (c,d) cross-sectional SEM images of bare Si and CoS_2-Si-250 microwire arrays.

X-ray diffraction (XRD) showed that CoS_2-Si MWs were consistent with pyrite CoS_2 structure (JCPDS 41-1471) with space group $Pa\bar{3}$, as shown in Figure 4a. The diffraction peaks at 2 theta values of 27.8°, 32.3°, 36.2°, 39.8°, and 54.9° corresponded to the Miller indices of (111), (200), (210), (211), (220), and (311), respectively. The diffraction peak intensity of Si MWs at ~62° reduced with increasing the thickness of CoS_2 layer, indicating a thicker passivation layer fully covered on underlying Si MWs. The crystal structure of the cubic pyrite-type CoS_2 was described by the $Pa\bar{3}$ (No. 205) space group, and its one unit cell is shown in Figure S4. Each cobalt cation was clearly surrounded by the six nearest sulfur anions to form a slightly distorted octahedron, and an S-S covalent bond was present between the two nearest-neighbor sulfur atoms. From an ionic perspective, CoS_2 can be regarded as a Co^{2+} ion plus one doubly charged S-S dimer. The calculated structural data are listed in Table S1 for comparison with the experimental results. After geometry optimization, the electronic band structure was calculated and shown in Figure S5. A half-metallic character was concluded from the calculated position of the Fermi energy level E_F, which was in good agreement with other band structure calculations previously reported. The traditional crystal field (CF) theory can be used to explain such a half-metallic behavior. Given that the ground CF configuration for the six-coordinated Co^{2+} cation should be $t_{2g}^6e_g^1$, a energy gap may be found between the fully-filled t_{2g} bands and empty e_g bands of "beta" electrons (with the down spin) because of the known t_{2g}-e_g CF splitting of the 3d electrons, whereas the single e_g electron occupation for "alpha" electrons (with the up spin) could obscure such a CF gap. The energy gap for beta electrons was calculated as 2.7261 eV. The calculated magnetic moment of each Co cation in one unit cell was 1 μB, thereby showing good agreement with both the experimental result (see Table S1) and prediction of CF theory. Reflectance spectroscopy revealed that the visible and near-infrared illumination (400–1100 nm) was absorbed by the pristine Si MWs, but the shorter wavelength (<400 nm) irradiation was reflected, as shown in Figure 4b. However,

decorating the CoS_2 layer on Si MWs reduced the reflectance of ultraviolent light. Notably, a higher thickness of the CoS_2 outer shell slightly blocked the Si inner cores for the absorption of incident light and decreased the amount of photogenerated carriers. Five Raman modes [A_g, E_g, $T_g(1)$, $T_g(2)$, and $T_g(3)$] of the CoS_2 structure were observed in Figure 5.[32] A_g mode was the in-phase stretching vibration of sulfur atoms in the dumbbells, but $T_g(2)$ was the out-of-phase stretching mode. E_g was the librational vibration of sulfur dumbbells. However, $T_g(1)$ and $T_g(3)$ modes corresponded to different compositions of stretching and librational vibration of sulfur atoms. The Raman spectrum of CoS_2-Si-200 MWs not only revealed the vibration modes of CoS_2 outer shell, but also the inner Si cores whose Raman shift was ~525 cm^{-1}, corresponding to the pristine Si MWs. This result indicated that the deposition of the CoS_2 layer on Si MWs had no negative effects on their surface. Upon increasing the loading amount of the CoS_2 layer by increasing its thickness to 250 nm, the Raman peak of Si MWs could not be observed, which showed that thicker CoS_2 outer shell had no pinholes to reveal underlying Si MWs and blocked the incident laser beam. This result was complementary to the data of the XRD and reflectance spectra.

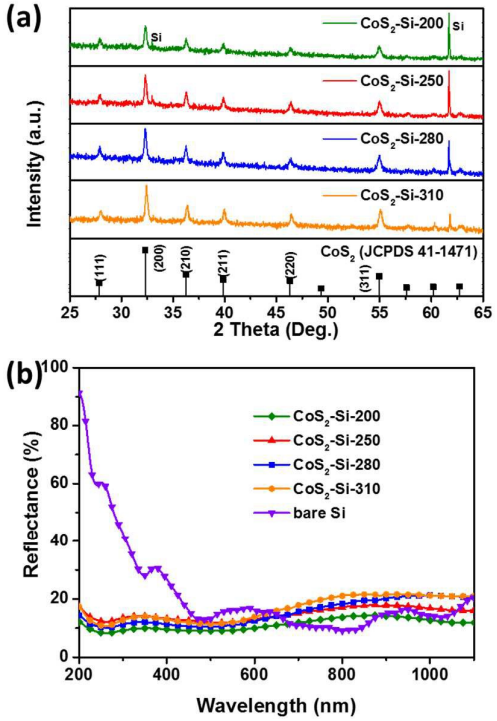

Fig. 4 (a) XRD and (b) reflectance spectra of CoS_2-Si microwire arrays with various CoS_2 thicknesses. All diffraction peaks matched the standard pattern of pyrite-phase CoS_2 (JCPDS No. 41-1471).

The three-electrode photoelectrochemical cell was applied to measure LSV of CoS_2-Si electrodes in 0.5 M H_2SO_4 aqueous solution under solar illumination (100 mW cm^{-2}), as shown in Figure 6a. The bare Si MWs showed no photoresponse at 0 V, but the photocurrent of the CoS_2-Si-200 electrode increased to −0.694 mA cm^{-2}. The pristine Si MWs showed photocatalytic activity until the applying bias was approximately −0.75 V, and its photocurrent at −0.85 V was −3.12 mA cm^{-2} in the inset of Figure 6a. The photocurrent was enhanced to −3.22 mA cm^{-2} at 0 V after Si MWs were coated by a CoS_2 layer with 250 nm thickness. However, further increasing the loading amount of the CoS_2 layer by prolonging the chemical deposition duration reduced the photocurrents of CoS_2-Si-280 and CoS_2-Si-310 electrodes to −2.01 and −1.57 mA cm^{-2} at 0 V, respectively. In order to identify whether the CoS_2 material is photoexcited, the controlled electrode was fabricated by synthesizing a CoS_2 layer on fluorine-doped tin oxide (FTO) glasses. CoS_2/FTO electrode was prepared through the same procedure as CoS_2-Si-250 MWs, and Figure S6 shows no impurity in the XRD spectra observed. In this study, the onset potential was defined as the voltage of the photocurrent reached −1.0 mA cm^{-2}. The onset potentials and current densities of the CoS_2/FTO electrode under dark condition and solar irradiation were exactly the same, as shown in Figure S7a. This result shows that the CoS_2 layer only functioned as a co-catalyst, accelerating the transfer photogenerated carriers from Si MWs to the interface with the electrolyte, instead of a photoabsorber. After iR correction from the R_s value of electrochemical impedance spectroscopy (EIS) characterization in Figure S7b, the onset potential of the CoS_2/FTO electrode was −0.146 V, and its current reached −28.3 mA cm^{-2} at −0.234 V. Figure S7c reveals the Tafel plot of the CoS_2/FTO electrode with iR correction. The classic two-electron reactions of HER mechanism can be described by two steps as follows: a discharging step of the Volmer reaction ($H_3O^+ + e^- \rightarrow H_{ads} + H_2O$) followed by a desorption step of the Heyrovsky reaction ($H_{ads} + H_3O^+ + e^- \rightarrow H_2 + H_2O$); or a recombination of the Tafel reaction ($H_{ads} + H_{ads} \rightarrow H_2$), where H_{ads} is indicated to the hydrogen atom adsorbed at the active site on the surface of catalyst. Moreover, the catalyst with the Tafel slope of 116, 38, or 29 mV dec^{-1} presented that the rate determining step in the HER process was the Volmer, Heyrovsky, or Tafel reaction, respectively. If the hydrogen atoms were weakly bonded to the surface of the catalyst, the adsorption step would limit the overall reaction rate. By contrast, as the hydrogen atoms were strongly bonded to the surface of the catalyst, the desorption step would restrict the overall reaction efficiency.[33] The CoS_2/FTO electrode with a Tafel slope of 61.9 mV dec^{-1} revealed that the CoS_2 layer might follow the Volmer-Heyrovsky mechanism, and rates of the discharge step and desorption step might be comparable during the HER process.[34]

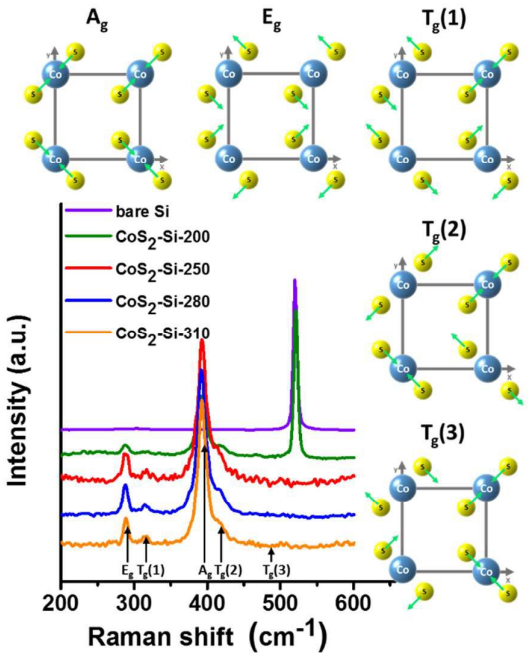

Fig. 5 Raman spectra of CoS_2-Si microwire arrays with various CoS_2 thicknesses, and schematic illustration of Raman vibration modes of CoS_2.

The transient currents of CoS_2-Si electrodes with various CoS_2 thicknesses were measured at 0 V under chopped illumination, as shown in Figure S8a. No photocurrent was generated by the bare Si MWs, which was complementary to the LSV result, as shown in the inset of Figure S8a. By contrast, all the CoS_2-Si electrodes showed transient switch-on characteristics under pulsed illumination. Besides, no overshot-photocurrent was observed in these CoS_2-Si MWs as the incident light was activated. This result demonstrated that photogenerated electrons did not accumulate on the surface of the electrodes, but efficiently transferred to the electrolyte through the co-catalyst assistance of the CoS_2 layer. In this study, the CoS_2-Si-250 electrode was selected to carry out incident photon-to-electron conversion efficiency (IPCE) at 0 V under solar simulation (100 mW cm^{-2}) because of its optimized photocatalytic activity, as shown in Figure S8b. The maximum efficiency of CoS_2-Si-250 MWs achieved 5.12% at a wavelength of 665 nm. Reflectance spectra show that the visible and near-infrared illumination was absorbed and UV incident light were reflected by Si MWs in Figure 4b. Besides, linear-sweep voltammogram measurement was conducted in Figure S7b to reveal that CoS_2 layer was functioned as a co-catalyst without contribution to photo-induced carriers. Therefore, the ICPE result of CoS_2-Si photocathode was detected between the wavelength under visible and near-infrared irradiation. Besides, previous studies of Si photoelectrode show the analogous IPCE results.[7, 35, 36]

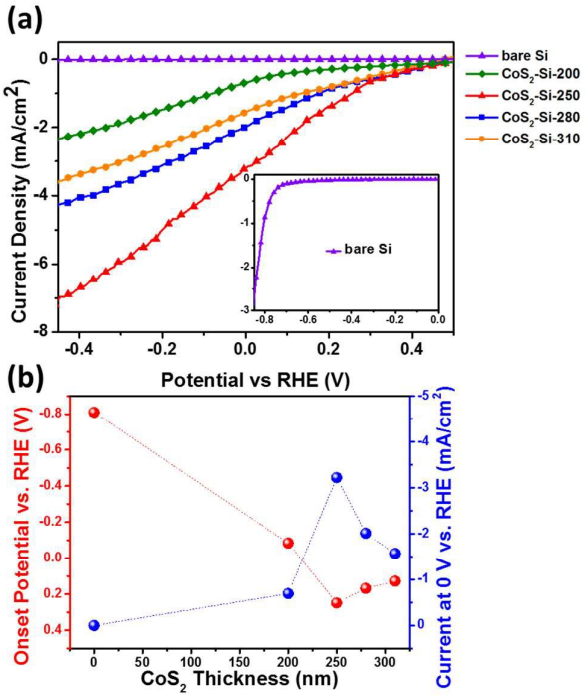

Fig. 6 (a) Linear-sweep voltammograms of CoS_2-Si electrodes with various CoS_2 thicknesses. The inset is linear sweep voltammogram of the bare Si electrode under more negative applied bias. (b) Onset potential and photocurrent versus CoS_2 thicknesses of CoS_2-Si electrodes.

Figure 6b shows variation in onset potential and photocurrent of CoS_2-Si electrodes with various CoS_2 thicknesses. The onset potential of pristine Si MWs was −0.810 V, but it positively shifted to −0.0844 V as the CoS_2 thickness modified on Si MWs was 200 nm. The improved-onset potential of CoS_2-Si-250 was saturated at 0.248 V, but CoS_2-Si-280 and CoS_2-Si-310 electrodes were decreased to 0.167 and 0.127 V, respectively. These results demonstrated that a thinner CoS_2 layer inefficiently ameliorated HER kinetics on the surfaces of Si MWs, but the excess loading amount of the CoS_2 outer shell also reduced the photocatalytic activity. The co-catalysts on photoelectrodes generally play three roles: passivation of surface traps, extraction of minority carriers and lower the energy barrier for redox reaction at the photoelectrode/electrolyte interface.[37] The surface of Si MWs retained high quality as shown in SEM images, because Si MWs was prepared through by photolithography and dry etching technique. The CoS_2 layer on Si MWs improved simultaneously the photocurrent and on-set potential, indicating that CoS_2 catalyst enhanced the kinetics of photo-induced carriers and reduced the possibility of recombination. Besides, the blocking absorption effect and charge transfer efficiency were the factors contributing to the onset potential improvement of Si MWs by modifying the CoS_2 co-catalyst.[38] The blocking absorption effect indicated that a thicker CoS_2 outer shell reduced the absorption of underlying Si inner core and decreased the amount of photoinduced carriers to

lower the photoresponse. However, the reflectance spectra in Figure 4b revealed a slight difference in the absorption of CoS_2-Si MWs with various decoration durations. This result indicated that the absorbing discrepancy of the CoS_2-Si electrodes with different CoS_2 loading amounts has no dominant role in photoelectrochemical performance. By contrast, the charge transfer efficiency, which might be the main factor in photoresponse, was related to the crystallization of the CoS_2 co-catalyst and resistances in the CoS_2-Si electrode. The crystallization of the CoS_2 outer shell influenced the recombination possibility of carriers generated by Si MWs, but the XRD spectra showed no evident difference between the CoS_2-Si electrodes in Figure 4a. Therefore, we proposed that the mainspring of the photocatalytic discrepancy resulted from the variation in charge transfer resistances between CoS_2-Si electrodes with various deposition times and the electrolyte.

In order to confirm the as-described hypothesis, EIS was conducted to analyse the charge transfer resistances among the photoabsorber, co-catalyst, and redox couples in the electrolyte. EIS characterization was carried out under solar illumination with an applied bias of 0.4 V in Figure 7a. The semicircle at high frequency was the charge transfer resistance ($R_{ct}1$) from underlying Si inner cores to CoS_2 outer shell, but the low frequency one ($R_{ct}2$) was from the CoS_2 layer to redox couples in the electrolyte, as shown in the schematic illustration in Figure 7b. The charge transfer resistances versus various CoS_2 thicknesses of CoS_2-Si electrodes are summarized in Figure 7c. Both charge transfer resistances of CoS_2-Si MWs were optimized as the thickness of CoS_2 layer reached 250 nm. The $R_{ct}2$ value was correlated with the catalytic activity of the CoS_2 outer shell.[39] The $R_{ct}2$ of CoS_2-Si-200 was 369 Ω cm^2 because of a lower HER kinetic improvement through a lower loading amount of the CoS_2 layer. By increasing the CoS_2 thickness to 250 nm, the $R_{ct}2$ value was dramatically reduced to 56.5 Ω cm^2. However, further increasing the loading amount of the CoS_2 layer by prolonging chemical deposition time led to higher $R_{ct}2$ values. This result indicated that a highly thick CoS_2 outer shell functioned as an electron-trapping center that enhanced longer diffusion length of photoinduced carriers to react with redox couples in the electrolyte and increased the probability of recombination. The $R_{ct}1$ value was related to the interfacial quality and electronic states between the CoS_2 layer and Si MWs. The CoS_2-Si electrodes were prepared by identical $Co(OH)_2$ deposition and thermal sulfidation methods, so we proposed that the interfacial quality was not the dominant affecting parameter of the $R_{ct}1$ value. Besides, the previous study reveals that lower $R_{ct}1$ was due to more available electronic states in the co-catalyst.[39] Therefore, the theoretical band structure calculation and X-ray absorption near-edge structure (XANES) were applied to resolve the electronic states of the CoS_2 outer shell.

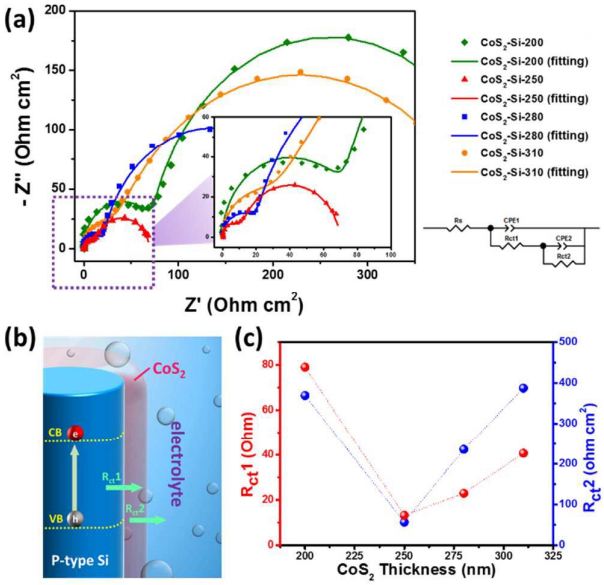

Fig. 7 (a) Electrochemical impedance spectroscopy of CoS_2-Si electrodes at 0.4 V bias under solar illumination. (b) Schematic illustration of charge transfer resistances between the composition materials of photoelectrode ($R_{ct}1$), and between the photoelectrode and redox couples in the electrolyte ($R_{ct}2$). (c) Charge transfer resistances versus CoS_2 thicknesses of CoS_2-Si electrodes.

The diagrams for calculated partial and total densities of states (PDOS/DOS) for CoS_2 are given in Figure S9. The known t_{2g}-e_g CF splitting could be found for the Co-3d states with both the up and down spins, which further confirmed our band structure analysis. The t_{2g} bands were considerably narrower than the very dispersive e_g bands. They were mainly located around −3.1 and −1.9 eV for alpha and beta electrons, respectively, so the exchange splitting for the t_{2g} states was estimated at 1.2 eV. The upper e_g band crossed the Fermi energy level with the width of 2.9 eV, whereas the lower e_g band was separated from the lower t_{2g} band by a energy gap of 3 eV. The Co-3d states were strongly hybridized with the S-3p states because of the strong overlap between each divalent cobalt ion and its nearest sulfur ligands, so a similar but more dispersive DOS pattern for the S-3p states was observed. The S-3d states were located at 6.8 eV and far away from the S-3p states. The S-3s states ranged from −19 eV to −12 eV and corresponded to the outermost core band consisting of two sub-bands with an energy separation of 3 eV.

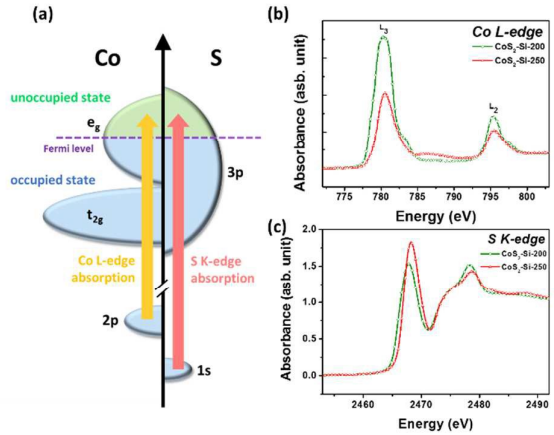

Fig. 8 (a) Schematic illustration of Co L-edge and S K-edge X-ray absorption spectra, and normalized XANES (b) Co L-edge and (c) S K-edge spectra.

According to a previous study, the density functional theory (DFT) calculation was carried out to reveal that the sulfur atoms of the pyrite catalyst were HER active sites.[40] Guo *et al.* prepared MoS_2–SiC hybrid electrocatalyst for hydrogen evolution.[41] The XPS spectra show the binding energy of C in the MoS_2–SiC shifted to a higher value in comparison with pristine SiC, indicating that surrounding electrons of C are transferred to other atoms. This result reveals that the electrons was accepted from C and rapidly transferred to Si and S active edges. Moreover, longer S-H_{ads} bond length on the pyrite catalyst with a weaker bond strength reduced the kinetic energy barrier by effectively promoting H–H bond formation. We proposed that the presence of more vacancies in the unoccupied states of CoS_2 to receive photogenerated electrons from Si MWs and enhance the photocatalytic activity. The theoretical calculation of band structure shows that the unoccupied electronic states of the CoS_2 layer were composed of Co-3d and S-3p orbitals. Therefore, Co L-edge and S K-edge XANES were used to investigate the unoccupied electronic states of the CoS_2 layer because the Co L-edge and S K-edge absorption, respectively, involved the transition from the 2p to 3d states and 1s to 3p states, as shown in Figure 8a. The stronger XANES intensity indicates the presence of more vacancies in the unoccupied states of CoS_2. In this study, CoS_2-Si-200 and CoS_2-Si-250 with the worst and optimized $R_{ct}1$ values were selected to conduct XANES analysis, as shown in Figures 8b and 8c. Two peaks in the Co L-edge spectrum of CoS_2 outer shell corresponded to L_2 (~795 eV) and L_3 (~780 eV) absorption. A shoulder at the L_3 peak shifted by approximately 4–8 eV, which indicated that transitions from Co-2p core level to empty Co-4s states were present.[42] The Co L_3 absorption intensity of CoS_2-Si-200 electrode, stronger than that of CoS_2-Si-250 MWs, showed that more vacancies were present in its unoccupied Co-3d states. By contrast, the S K-edge jump of CoS_2-Si-250 electrode was higher than that of CoS_2-Si-200 MWs. This result revealed an opposite trend, which presented more empty states in the S-3p orbital of the CoS_2-Si-250 electrode. The theoretical calculation of the electronic states showed that the Co-3d and S-3p states were strongly hybridized. Therefore, more vacancies in the unoccupied states of the CoS_2 layer normally simultaneously enhance both Co L-edge and S K-edge absorption. We proposed that the reversed tendency of Co L-edge and S K-edge absorption intensity, observed in CoS_2-Si electrodes, indicated a charge transfer between Co and S atoms of CoS_2-Si-250 MWs. The S atoms of the CoS_2-Si-250 electrode, donating electrons to empty states in Co-3d orbital, generated more vacancies in unoccupied states of S-3p orbital. This result leads to more photoinduced-electrons from Si MWs of CoS_2-Si-250 electrode that could be accepted through the S atoms and further transferred to the S active sites on the surface of CoS_2 for the solar hydrogen generation reaction. Moreover, Figure 8c also shows that the S K-edge absorption of CoS_2-Si-250 MWs slightly shifted to higher energy. This result indicated that the CoS_2-Si-250 electrode presented a lower negative charge of S_2^{2-} and formed a weaker S-H_{ads} bond strength to promote water splitting efficiency.

The previous work of Ding *et al.* reveal that there was ohmic contact between metallic MoS_2 and Si.[39] However, the work function of CoS_2 was about 5.5 eV (vs. vacuum level),[43] and the fermi level of p-Si (resistivity: 10 Ω cm) was 4.9 eV.[44] After the band alignment, Figure 9a shows that there was a small barrier for photo-generated carriers migrating to the surface of photocathode, leading to lower photocurrent and fill factor, as compared with MoS_2-Si photoelectrode materials. Moreover, based on the studies of MoS_2-Si PEC devices,[39, 45-47] the resistivity of utilized-Si wafer was lower as compared to our research. Si photocathode with lower resistance improved the diffusion length of photo-induced carriers and further reduced the possibility of recombination. The X-ray photoelectron spectroscopy (XPS) spectra were applied to reveal that the SiO_2 thickness between CoS_2 shell and Si MWs during the chemical deposition process of $Co(OH)_2$ layer, owning to the exposure of aqueous reaction solution. To detect the underlying Si MWs of CoS_2-Si electrodes, Ar ion etching was applied to remove the CoS_2 outer shell until the intensity of the Si 2p peak no longer increased in Figure 9b. The Si/SiO_2 ratio of CoS_2-Si-250 photocathode was ~3.30, as shown in Figure 9c. The XPS spectra reveal that Si/SiO_2 ratios of CoS_2-Si-200 and CoS_2-Si-310 MWs, prepared under the shortest and longest exposure duration to aqueous reaction solution, were respectively about 4.87 and 2.07 in Figure S10. This result show that thickness of SiO_2 layer increased as longer chemical deposition time. The thicker SiO_2 layer of CoS_2-Si-310 blocked photo-induced carriers for transferring to the surface of photocathode. Although the oxide layer generating on CoS_2-Si-200 was thinner, the less loading amount of CoS_2 was unable to accelerate the kinetics of solar hydrogen evolution. According to above discussions, the water splitting efficiency of CoS_2-Si photocathode material can be further enhanced through using low resistivity Si MWs and reducing the formation of SiO_2 layer.

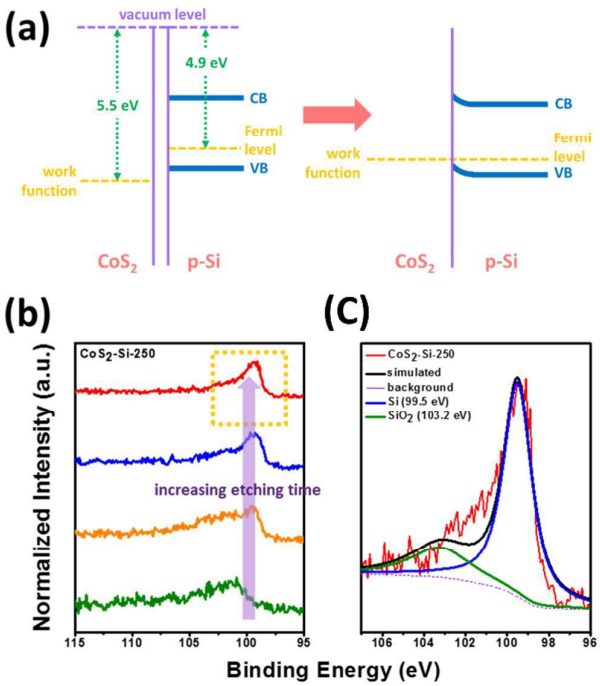

Fig. 9 (a) Band alignment diagram between CoS_2 and Si materials. High-resolution Si 2p spectra of as-prepared CoS_2-Si-250 electrode (b) with increasing Ar ion etching time and (c) different coordination conditions.

In this study, LSV measurements were carried out 30 times to analyze the stability of photocathodes. The scanned photocurrent of pristine Si MWs was −3.12 mA cm^{-2} at −0.85 V, but gradually decayed to −0.0882 mA cm^{-2}, which only retained ~2.83% of the initial photocurrent, after the 30th scanning measurement in Figure S11a. Besides, the onset potential of Si MWs reduced to −0.85 V after the fifth scanning test, but the consecutive scans must be applied more negative bias to attain −1.0 mA cm^{-2}, as shown in Figure S11c. The CoS_2-Si-250 electrode was selected for this characterization because of its optimal photoelectrochemical performance. Both onset potential and photocurrent of the CoS_2-Si-250 electrode revealed no degradation during the scanning test in Figure 10a and 10b. This result indicated that the CoS_2 co-catalyst effectively functioned as a passivation layer to defend Si MWs from oxidation in the electrolyte. Pt nanoparticle (NP)-modified Si MWs (Pt-Si) were also prepared through chemical electroless deposition for comparing the protective effects with the CoS_2-Si electrode. The onset potential and photocurrent of the Pt-Si electrode were 0.0868 V and −3.53 mA cm^{-2} at 0 V, respectively, as shown in Figure S11b. The photocurrent of the Pt-Si electrodes reached saturation after applying bias above −0.2 V, because of the limited ion diffusion rate of the electrolyte or electron conducting rate of the Si MWs. The fifth scanned onset potential and photocurrent of the Pt-Si electrode decreased to 0.0666 V and −3.03 mA cm^{-2} at 0 V. After scanning for 30 times, the onset potential of Pt-Si MWs was maintained at 0.0364 V, and the retention of the initial onset potential was only approximately 41.9% in Figure S11d. Besides, the 30th scanned photocurrent gradually reduced to −1.99 mA cm^{-2} at 0 V. This result demonstrated that Pt NPs, which only functioned as a co-catalyst, efficiently transferred the photoinduced carriers to the interface and reduced recombination. However, Pt NPs were unable to prevent the Si MWs from durability degradation because of oxidation. Further increasing the loading amount of Pt NPs to fully cover the surface of Si MWs using the prolonged electroless deposition duration possibly improved its photocatalytic stability. However, the high expense of Pt NPs limited its practical utilization, and excess Pt NPs also blocked the absorption of underlying Si MWs to reduce the photoelectrochemical performance. Besides, high loading amounts of Pt NPs on Si MWs might also serve as trapping centers to increase the probability of recombination.

XPS spectra were conducted not only to investigate the stability of CoS_2 passivation layer, but also to characterize whether the oxide layer formation on Si MWs leads to photocatalytic decay after the LSV measurement. Figure S12a shows the XPS spectra of the CoS_2-Si electrodes with various CoS_2 thicknesses. Notably, no Si peaks were observed in the spectra. This result indicated that the CoS_2 layer was completely coated on the entire surface of Si MWs without pinholes or cracks. High-resolution Co 2p XPS spectra in Figure S12b revealed two peaks originated from Co-2$p_{3/2}$ and 2$p_{1/2}$ of CoS_2 layer at 778.8 and 794.0 eV. There was a broad band of CoS_2 layer at ~162 eV in S 2p XPS spectra. Besides, Figure S12b revealed no satellite peaks at 780.9 and 797.8 eV in the Co 2p spectra, as well as the sulfate peak at 168.7 eV in the S 2p spectra, indicating that the CoS_2 layer was stable without oxidation in air or even after 30 LSV scans (purple curves in Figure S12b).[22] The XPS Si 2p region of the bare Si and Pt-Si electrode showed two peaks with binding energies of 99.5 and 103.2 eV, separately ascribed from the Si MWs and SiO_2 oxide layer, respectively, as shown in Figure S13. The Si/SiO_2 ratios of the bare Si and Pt-Si MWs were approximately 0.708 and 1.33, respectively, but the ratios decreased to 0.511 and 0.567, respectively, after 30 LSV scans characterization. This result revealed that Si MWs oxidized to the insulating SiO_2 layer to enhance the possibility of recombination and result in serious photoelectrochemical degradation in Figure S11. Notably, the SiO_2 peak of the CoS_2-Si-250 electrode did not enhance after 30 LSV scans, as shown in Figure 9c and S14. Thus, the CoS_2 passivation layer was extremely robust to stand up to the electrolyte from self-oxidation. Besides, the CoS_2 outer shell fully covered the surface of Si inner core to prevent oxidation formation during the photoelectrochemcial reaction. These factors predominantly contributed to the considerably higher photocatalytic stability of CoS_2-Si electrodes compared with pristine Si and Pt-Si electrodes.

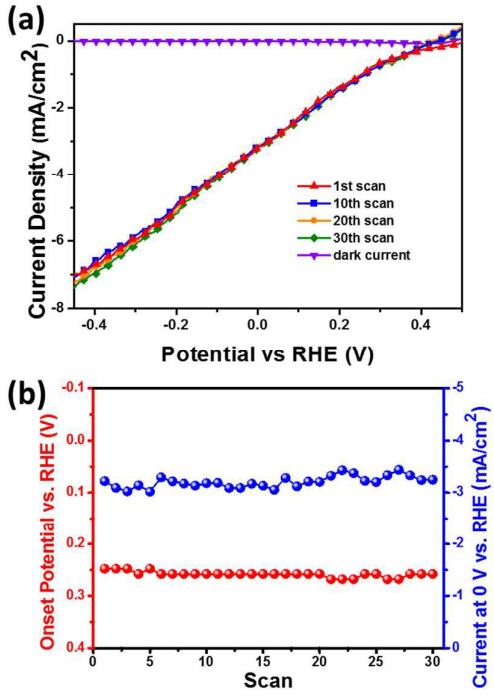

Fig. 10 (a) Linear-sweep voltammograms of CoS_2-Si-250 electrode scanned for 30 times, and (b) onset potential and photocurrent of CoS_2-Si electrode versus scan times.

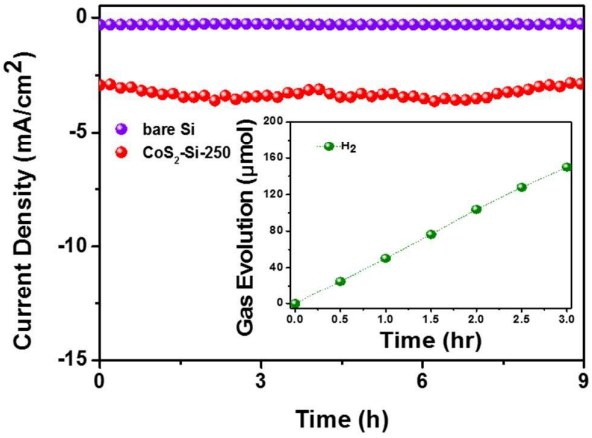

Fig. 11 Chronoamperometry of bare Si and CoS_2-Si-250 electrodes under solar irradiation at 0 V, and the inset is the gas evolution of CoS_2-Si-250 electrode under solar irradiation at 0 V.

Chronoamperometry was conducted at 0 V under solar illumination. The photocurrent of the CoS_2-Si-250 electrode was stably retained at -3 mA cm^{-2} for 9 h in Figure 11. This finding indicated that the CoS_2 passivation layer was not only extremely stable to overcome self-oxidation, but also robust to protect underlying Si MWs from oxidation leading to serious recombination of photoinduced carriers. Moreover, no photoresponse was observed from the bare Si electrode in Figure 11, which revealed that the current of CoS_2-Si-250 MWs did not contribute from the dark current or irreversible side reaction during the 9 h chronoamperometric measurement. The CoS_2 layer efficiently transferred minority carriers of Si MWs to the interfaces with the electrolyte and reacted with protons to generate hydrogen gas through the co-catalyst effect. The gas evolution of the CoS_2-Si-250 electrode (the area was ~1 cm^2) was characterized at 0 V under solar illumination, as shown in the inset of Figure 11. The hydrogen generation rates were 0.833. In addition, the faradic efficiencies of hydrogen was 83.2%.

Conclusions

In summary, we developed a CoS_2 co-catalyst passivation layer-modified Si MWs photocathode for water splitting. The optimized onset potential and photocurrent of the CoS_2-Si electrode reached 0.248 V and -3.22 mA cm^{-2} (at 0 V), respectively, as the thickness of CoS_2 was 250 nm. The low charge transfer resistances of CoS_2-Si-250 MWs among the photoabsorber, co-catalyst, and redox couples in the electrolyte led to high photoelectrochemical activity. Moreover, the XANES spectra revealed that more vacancies in the unoccupied S-3p states of the CoS_2-Si-250 electrode were present, which functioned as active sites of water splitting, accepting more photogenerated electrons from Si MWs. The lower negative charged S_2^{2-} of CoS_2-Si-250 MWs also reduced the bond strength of S-H_{ads} and promoted its water splitting efficiency. The CoS_2 outer shell on Si MWs showed a stable characteristic without self-oxidation after the photocatalytic measurement, which was observed through the XPS spectra. Moreover, the CoS_2 co-catalyst functioned as a robust passivation layer and inhibited the oxidation of Si MWs to further prevent the degradation of photocatalytic activity. The CoS_2-Si-250 MWs maintained the photocurrent at -3 mA cm^{-2} (at 0 V) for 9 h, and its hydrogen generation rate was approximately 0.833 μmol min^{-1}, respectively.

Acknowledgements

The authors are grateful for the financial support of the Ministry of Science, Technology of Taiwan (Contract No. MOST 103-2112-M-003-009-MY3 and MOST 104-2113-M-002-012-MY3), and Academia Sinica (Contract No. AS-103-TP-A06). C.-G. Ma appreciates the financial support from National Natural Science Foundation of China (Grant No. 11204393) and Natural Science Foundation of Chongqing (Grant No. CSTC2014JCYJA50034).

Notes and references

1. R. E. Blankenship, D. M. Tiede, J. Barber, G. W. Brudvig, G. Fleming, M. Ghirardi, M. R. Gunner, W. Junge, D. M. Kramer, A. Melis, T. A. Moore, C. C. Moser, D. G. Nocera, A. J. Nozik, D. R. Ort, W. W. Parson, R. C. Prince and R. T. Sayre, *Science*, 2011, **332**, 805-809.
2. S. N. Habisreutinger, L. Schmidt-Mende and J. K. Stolarczyk, *Angew.Chem. Int. Edit.*, 2013, **52**, 7372-7408.
3. A. Fujishima and K. Honda, *Nature*, 1972, **238**, 37-+.

4. S. W. Boettcher, E. L. Warren, M. C. Putnam, E. A. Santori, D. Turner-Evans, M. D. Kelzenberg, M. G. Walter, J. R. McKone, B. S. Brunschwig, H. A. Atwater and N. S. Lewis, *J. Am. Chem. Soc.*, 2011, **133**, 1216-1219.
5. I. Oh, J. Kye and S. Hwang, *Nano Lett.*, 2012, **12**, 298-302.
6. P. Dai, J. Xie, M. T. Mayer, X. Yang, J. Zhan and D. Wang, *Angew. Chem. Int. Edit.*, 2013, **52**, 11119-11123.
7. C. J. Chen, M. G. Chen, C. K. Chen, P. C. Wu, P. T. Chen, M. Basu, S. F. Hu, D. P. Tsai and R. S. Liu, *Chem. Commun.*, 2015, **51**, 549-552.
8. J. R. McKone, N. S. Lewis and H. B. Gray, *Chem. Mater.*, 2014, **26**, 407-414.
9. J. R. McKone, E. L. Warren, M. J. Bierman, S. W. Boettcher, B. S. Brunschwig, N. S. Lewis and H. B. Gray, *Energ. Environ. Sci.*, 2011, **4**, 3573-3583.
10. E. L. Warren, J. R. McKone, H. A. Atwater, H. B. Gray and N. S. Lewis, *Energ. Environ. Sci.*, 2012, **5**, 9653-9661.
11. M. Basu, Z. W. Zhang, C. J. Chen, P. T. Chen, K. C. Yang, C.-G. Ma, C. C. Lin, S. F. Hu and R. S. Liu, *Angew.Chem. Int. Edit.*, 2015, **54**, 6211-6216.
12. B. Seger, T. Pedersen, A. B. Laursen, P. C. K. Vesborg, O. Hansen and I. Chorkendorff, *J. Am. Chem. Soc.*, 2013, **135**, 1057-1064.
13. H. Haick, P. T. Hurley, A. I. Hochbaum, P. Yang and N. S. Lewis, *J. Am. Chem. Soc.*, 2006, **128**, 8990-8991.
14. L. E. O'Leary, E. Johansson, B. S. Brunschwig and N. S. Lewis, *J. Phys. Chem. B*, 2010, **114**, 14298-14302.
15. U. Sim, T.-Y. Yang, J. Moon, J. An, J. Hwang, J.-H. Seo, J. Lee, K. Y. Kim, J. Lee, S. Han, B. H. Hong and K. T. Nam, *Energ. Environ. Sci.*, 2013, **6**, 3658-3664.
16. B. Seger, A. B. Laursen, P. C. K. Vesborg, T. Pedersen, O. Hansen, S. Dahl and I. Chorkendorff, *Angew. Chem. Int. Edit.*, 2012, **51**, 9128-9131.
17. A. B. Laursen, T. Pedersen, P. Malacrida, B. Seger, O. Hansen, P. C. K. Vesborg and I. Chorkendorff, *Phys. Chem. Chem. Phys.*, 2013, **15**, 20000-20004.
18. X. Zhang, F. Meng, S. Mao, Q. Ding, M. J. Shearer, M. S. Faber, J. Chen, R. J. Hamers and S. Jin, *Energ. Environ. Sci.*, 2015, **8**, 862-868.
19. M. S. Faber and S. Jin, *Energ. Environ. Sci.*, 2014, **7**, 3519-3542.
20. D. Kong, J. J. Cha, H. Wang, H. R. Lee and Y. Cui, *Energ. Environ. Sci.*, 2013, **6**, 3553-3558.
21. A. Ivanovskaya, N. Singh, R.-F. Liu, H. Kreutzer, J. Baltrusaitis, N. Trung Van, H. Metiu and E. McFarland, *Langmuir*, 2013, **29**, 480-492.
22. M. S. Faber, R. Dziedzic, M. A. Lukowski, N. S. Kaiser, Q. Ding and S. Jin, *J. Am. Chem. Soc.*, 2014, **136**, 10053-10061.
23. D. Kong, H. Wang, Z. Lu and Y. Cui, *J. Am. Chem. Soc.*, 2014, **136**, 4897-4900.
24. M. S. Faber, M. A. Lukowski, Q. Ding, N. S. Kaiser and S. Jin, *J. Phys. Chem. C*, 2014, **118**, 21347-21356.
25. Y. Sun, C. Liu, D. C. Grauer, J. Yano, J. R. Long, P. Yang and C. J. Chang, *J. Am. Chem. Soc.*, 2013, **135**, 17699-17702.
26. R. Dovesi, V. R. Saunders, C. Roetti, R. Orlando, C. M. Zicovich-Wilson, F. Pascale, B. Civalleri, K. Doll, N. M. Harrison, I. J. Bush, P. D'Arco and M. Llunell, CRYSTAL09 User's Manual, University of Torino: Torino, 2009.
27. R. Demichelis, B. Civalleri, M. Ferrabone and R. Dovesi, *Int. J. Quantum Chem.*, 2010, **110**, 406-415.
28. R. Dovesi, F. F. Fava, C. Roetti and V. R. Saunders, *Faraday Discuss.*, 1997, **106**, 173-187.
29. T. Homann, U. Hotje, M. Binnewies, A. Borger, K. D. Becker and T. Bredow, *Solid State Sci.*, 2006, **8**, 44-49.
30. C. G. Ma and M. G. Brik, *Comp. Mater. Sci.*, 2012, **58**, 101-112.
31. H. J. Monkhorst and J. D. Pack, *Phys. Rev. B*, 1976, **13**, 5188-5192.
32. S. G. Lyapin, A. N. Utyuzh, A. E. Petrova, A. P. Novikov, T. A. Lograsso and S. M. Stishov, *J. Phys.-Condens. Mat.*, 2014, **26**.
33. J. D. Benck, T. R. Hellstern, J. Kibsgaard, P. Chakthranont and T. F. Jaramillo, *ACS Catal.*, 2014, **4**, 3957-3971.
34. Z. Huang, Z. Chen, Z. Chen, C. Lv, H. Meng and C. Zhang, *ACS Nano*, 2014, **8**, 8121-8129.
35. A. Kargar, K. Sun, Y. Jing, C. Choi, H. Jeong, G. Y. Jung, S. Jin and D. Wang, *ACS Nano*, 2013, **7**, 9407-9415.
36. A. Kargar, K. Sun, Y. Jing, C. Choi, H. Jeong, Y. Zhou, K. Madsen, P. Naughton, S. Jin, G. Y. Jung and D. Wang, *Nano Lett.*, 2013, **13**, 3017-3022.
37. J. Li and N. Wu, *Catal. Sci. Technol.*, 2015, **5**, 1360-1384.
38. H. M. Chen, C. K. Chen, C. J. Chen, L. C. Cheng, P. C. Wu, B. H. Cheng, Y. Z. Ho, M. L. Tseng, Y. Y. Hsu, T. S. Chan, J. F. Lee, R. S. Liu and D. P. Tsai, *ACS Nano*, 2012, **6**, 7362-7372.
39. Q. Ding, F. Meng, C. R. English, M. Cabán-Acevedo, M. J. Shearer, D. Liang, A. S. Daniel, R. J. Hamers and S. Jin, *J. Am. Chem. Soc.*, 2014, **136**, 8504-8507.
40. D.-Y. Wang, M. Gong, H.-L. Chou, C.-J. Pan, H.-A. Chen, Y. Wu, M.-C. Lin, M. Guan, J. Yang, C.-W. Chen, Y.-L. Wang, B.-J. Hwang, C.-C. Chen and H. Dai, *J. Am. Chem. Soc.*, 2015, **137**, 1587-1592.
41. X. Guo, X. Tong, Y. Wang, C. Chen, G. Jin and X.-Y. Guo, *J. Mater. Chem. A*, 2013, **1**, 4657-4661.
42. V. N. Antonov, O. V. Andryushchenko, A. P. Shpak, A. N. Yaresko and O. Jepsen, *Phys. Rev. B*, 2008, **78**.
43. Y. Xu and M. A. A. Schoonen, American Mineralogist, 2000, 85, 543-556.
44. I. Kentaro, A. Tomoki and K. Hikaru, *Materials Research Express*, 2015, **2**, 075901.
45. B. Seger, A. B. Laursen, P. C. K. Vesborg, T. Pedersen, O. Hansen, S. Dahl and I. Chorkendorff, *Angew. Chem. Int. Edit.*, 2012, **51**, 9128-9131.
46. A. B. Laursen, T. Pedersen, P. Malacrida, B. Seger, O. Hansen, P. C. K. Vesborg and I. Chorkendorff, *Phys. Chem. Chem. Phys.*, 2013, **15**, 20000-20004.
47. L. Zhang, C. Liu, A. Wong, J. Resasco and P. Yang, *Nano Res.*, 2015, **8**, 281-287.

TOC

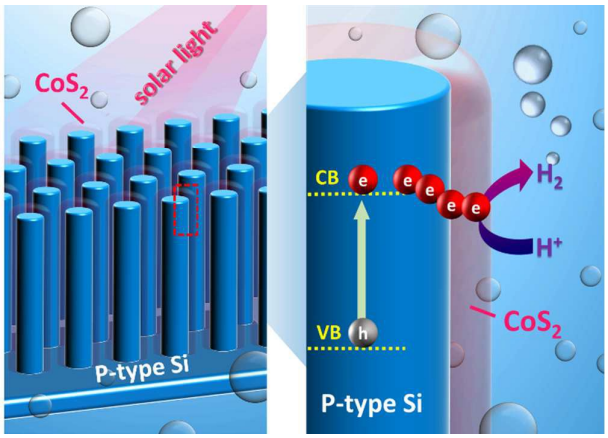

Integrated cobalt disulfide (CoS_2) co-catalytic passivation layer on Si microwires were used as a photocathode for solar hydrogen evolution. CoS_2-Si electrode showed the stable photocurrent at −3 mA cm^{-2} at 0 V for 9 h.